Inorganic Chemistry
Cite This: Inorg. Chem. 2019, 58, 1607−1620
Article
pubs.acs.org/IC

Partial and Complete Substitution of the 1,4-Benzenedicarboxylate Linker in UiO-66 with 1,4-Naphthalenedicarboxylate: Synthesis, Characterization, and H_2-Adsorption Properties

Vera V. Butova,*[,†] Andriy P. Budnyk,[†] Konstantin M. Charykov,[†] Kristina S. Vetlitsyna-Novikova,[†] Aram L. Bugaev,[†] Alexander A. Guda,[†] Alessandro Damin,[‡] Sachin M. Chavan,[§] Sigurd Øien-Ødegaard,[∥] Karl Petter Lillerud,[∥] Alexander V. Soldatov,[†] and Carlo Lamberti*[,†,⊥]

[†]The Smart Materials Research Institute, Southern Federal University, Sladkova Street 178/24, Rostov-on-Don 344090, Russia
[‡]Department of Chemistry, INSTM Reference Center and NIS Interdepartmental Center, and [⊥]Department of Physics, INSTM Reference Center and CrisDi Interdepartmental Center, University of Turin, Via P. Giuria 1, Turin 10125, Italy
[§]ProfMOF AS, Kirkegårdsveien 45, Kongsberg 3616, Norway
[∥]Centre for Materials Science and Nanotechnology, Department of Chemistry, University of Oslo, Sem Saelands vei 26, Oslo 0315, Norway

Supporting Information

ABSTRACT: We describe the synthesis and corresponding full characterization of the set of UiO-66 metal−organic frameworks (MOFs) with 1,4-benzenedicarboxylate ($C_6H_4(COOH)_2$, hereafter H_2BDC) and 1,4-naphthalenedicarboxylate ($C_{10}H_6(COOH)_2$, hereafter H_2NDC) mixed linkers with NDC contents of 0, 25, 50, and 100%. Their structural (powder X-ray diffraction, PXRD), adsorptive (N_2, H_2, and CO_2), vibrational (IR/Raman), and thermal stability (thermogravimetric analysis, TGA) properties quantitatively correlate with the NDC content in the material. The UiO-66 phase topology is conserved at all relative fractions of BDC/NDC. The comparison between the synchrotron radiation PXRD and 77 K N_2-adsorption isotherms obtained on the 50:50 BDC/NDC sample and on a mechanical mixture of the pure BDC and NDC samples univocally proves that in the mixed linkers of the MOFs the BDC and NDC linkers are shared in each MOF crystal, discarding the hypothesis of two independent phases, where each crystal contains only BDC or NDC linkers. The careful tuning of the NDC content opens a way for controlled alteration of the sorption properties of the resulting material as testified by the H_2-adsorption experiments, showing that the relative ranking of the materials in H_2 adsorption is different in different equilibrium-pressure ranges: at low pressures, 100NDC is the most efficient sample, while with increasing pressure, its relative performance progressively declines; at high pressures, the ranking follows the BDC content, reflecting the larger internal pore volume available in the MOFs with a higher fraction of smaller linkers. The H_2-adsorption isotherms normalized by the sample Brunauer−Emmett−Teller specific surface area show, in the whole pressure range, that the surface-area-specific H_2-adsorption capabilities in UiO-66 MOFs increase progressively with increasing NDC content. Density functional theory calculations, using the hybrid B3LYP exchange correlation functional and quadruple-ζ with four polarization functions (QZ4P) basis set, show that the interaction of H_2 with the H_2NDC linker results in an adsorption energy larger by about 15% with respect to that calculated for adsorption on the H_2BDC linker.

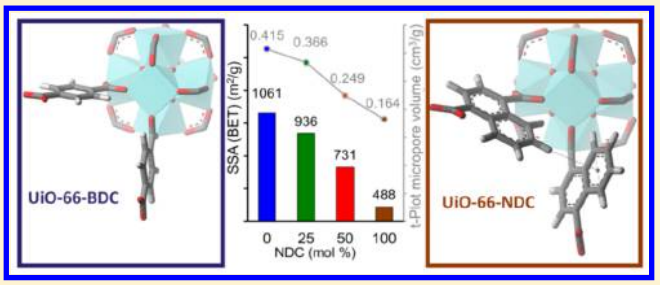

1. INTRODUCTION

Metal−organic frameworks (MOFs) are porous materials that have recently attracted much attention because of their tunable properties and therefore variety of applications.[1−19] According to Yaghi and co-workers,[20] there are two parts constructing the MOF structure: secondary building units (SBUs) and linkers. The geometry of the SBUs is defined by points of extension; they may contain one or several metal sites. The organic molecules—linkers—connect SBUs into a 3D framework. The choice of SBUs and linkers determines the topology and symmetry of the resulting MOF.[21] The endless number of possible SBUs and linkers leads to a great variety of MOF types. This wide field of molecular design is one of the reasons why MOFs are so popular nowadays. On the other hand, some families of MOFs have shown outstanding properties, making them attractive materials for many applications. For example, MOFs of the UiO-66 (named after the University of Oslo) series are known for their high thermal and chemical stability[22−25] and exceptional tolerance to structural defects

Received: November 7, 2018
Published: January 9, 2019

DOI: 10.1021/acs.inorgchem.8b03087
Inorg. Chem. 2019, 58, 1607−1620

Table 1. Molar Ratios of Reagents for Synthesis of the Samples and Main Characteristic Parameters

sample designation[a]	$ZrCl_4$ (mol)	H_2O (mol)	DMF (mol)	NDC (mol)	BDC (mol)	a[b] (Å)	SSA[c] (m^2/g)	pore volume (cm^3/g)	TGA peak[d] (°C)
0NDC (i.e., UiO-66)	1	3	300	0	1	20.7582(4)	1061	0.415	535
25NDC	1	3	300	0.25	0.75	20.7948(3)	936	0.366	525
50NDC	1	3	300	0.5	0.5	20.8285(5)	731	0.249	500
100NDC	1	3	300	1	0	20.8538(8)	488	0.164	480

[a]Designation of samples reflects the fraction in molar percent of NDC in the NDC/BDC linker mixture used in the synthesis batch. [b]Obtained from the Rietveld refinement of laboratory PXRD data. [c]Obtained using the BET theory. [d]Maximum value of the first-derivative peak in the TGA plots.

(like missing linkers or SBUs).[26,27] UiO-66 consists of $Zr_6O_4(OH)_4$ SBUs connected to each other by 1,4-benzenedicarboxylate (BDC) linkers.[22−24,28] There are a few ways to affect its properties without alternating the structure: substitution of the BDC linker with another one possessing the same connecting functionalities;[29−34] injection of a modulator to moderate the growth process;[35−38] functionalization of the linkers by side functional groups;[39−46] substitution in the SBU of the Zr(IV) metal cation with Hf(IV),[47−49] Ce(IV),[49−53] or Ti(IV)[54−58] metal cation, cooperative cluster metalation, and ligand migration;[59] etc. In our recent work,[60] we replaced the BDC linker with the 1,4-naphthalenedicarboxylate (NDC) one and introduced benzoic acid into the reaction mixture as a modulator. We demonstrated that full substitution of BDC linkers with NDC analogues did not change the framework topology. The introduction of benzoic acid resulted in bigger crystallites of improved morphology. The modulator's competitive linkage to SBUs led to a higher defect density (rising to almost 50%, depending on the quantity of the modulator) in the final material, characterized by increased specific surface area (SSA) and decreased thermal stability.

The partial substitution of linkers or the use of two or more types of different linkers in the same synthesis provides an additional degree of freedom in the synthesis, which could significantly change the properties of the product. MOFs with mixed linkers attracted much attention in the last years[61−64] because the resulting properties could not only result in simply linear sums of the pure-component properties but also have a synergetic effect in enhancing some specific properties. For example, Deng et al.[62] reported on a MOF-5-type structure with a mixture of three linkers, BDC-NO_2, BDC-$(OC_3H_5)_2$, and BDC-$(OC_7H_7)_2$, which exhibits up to 400% better uptake selectivity for carbon dioxide (CO_2) over carbon monoxide (CO). The main problem in the mixed-linker MOF synthesis is obtaining a single-phase material with mixed linkers instead of a mixture of phases, each with a single linker. In the present work, we have investigated the set of compositions of UiO-66-type MOFs with partial substitution of the BDC linker with the NDC one and proven that the BDC and NDC linkers are shared in each MOF crystal.

2. EXPERIMENTAL METHODS

2.1. Synthesis. The chemicals zirconium tetrachloride ($ZrCl_4$), 1,4-benzenedicarboxylic acid [H_2BDC, $C_6H_4(CO_2H)_2$], 1,4-naphthalenedicarboxylic acid [H_2NDC, $C_{10}H_6(CO_2H)_2$], *N*,*N*-dimethylformamide [DMF; $(CH_3)_2NC(O)H$], and tetrahydrofuran (THF, C_4H_8O), all of analytical grade, were obtained from commercial suppliers and used as received. Deionized (DI) water (18 MΩ·cm) was obtained from a Milli-Q ultrapure water system.

In a typical synthesis, $ZrCl_4$ (0.250 g) was dissolved in 25 mL of DMF in a conical flask, and then 57.9 μL of DI water was added to reach a molar ratio of 1:3:300 $ZrCl_4/H_2O$/DMF. After that, respective amounts of H_2BDC and H_2NDC were added under stirring to produce four samples with different molar ratio, as given in Table 1. After complete dissolution of the reagents has been reached, the reaction flask was sealed and placed in a preheated oven at 120 °C for 24 h. Crystallization was performed under static conditions. After cooling to room temperature, the resulting white solid was separated by centrifugation, washed twice with DMF and then once with THF, and dried at 60 °C in a conventional oven.

2.2. Characterization. The phase purity of the UiO samples was first determined by means of a laboratory-level powder X-ray diffraction (PXRD) D2 Phaser system (Bruker) operating with Cu Kα radiation (λ = 1.5418 Å). The 2θ = 5−60° data range was collected at step intervals of 0.02° with 0.1 s counting time per step. High-resolution diffraction patterns for profile analysis were then measured in 0.7 mm rotating glass capillaries at the Swiss−Norwegian Beamline (BM01B)[65] of the European Synchrotron Radiation Facility (ESRF), Grenoble, France. Capillaries were filled and sealed in air. For each sample, 15 2D diffraction images were recorded with 5 s acquisition time by the CMOS-Dexela 2D detector. The same number of dark images was recorded for background subtraction. Both the wavelength λ = 0.51353(1) Å and the sample-to-detector distance were calibrated using LaB_6 and silicon powder model samples from the National Institute of Standards and Technology. The adopted experimental setup allowed us to cover the 2θ = 2.0−32.0° range. In the refinements, we used the shorter interval of 2θ = 4.5−31.0° range, which corresponds to the Q range from 0.30 to 8.51 $Å^{-1}$ and to a d spacing ranging from 6.54 to 0.96 Å. Subsequent averaging and integration were carried out using the ESRF *PyFAI* software.[66] Further profile analysis was done using *Jana2006* software.[67]

The SSA and porosity were determined by the Brunauer−Emmett−Teller (BET) method[68] from the N_2-physisorption isotherm obtained (at −196 °C) on an ASAP 2020 (accelerated surface area and porosimetry) analyzer (Micromeritics). The sample was activated at 200 °C for 24 h in a dynamic vacuum before the measurement. The Barrett−Joyner−Halenda model[69] was used for pore-size distribution.

Raman spectra were recorded on a Renishaw Micro Raman instrument using 005% power of a 785 nm laser. Spectra were averaged on three different points, each measured with a 10× objective and 20 acquisitions. Fourier transform infrared (FTIR) spectra were recorded in transmission mode on a Vertex 70 (Bruker) spectrometer with a resolution of 2 cm^{-1}. Determination of the linker vibrational modes was performed on samples prepared with the KBr pelleting technique. Conversely, measurements of the CO_2 adsorption at room temperature were performed on the samples compacted in self-supporting pellets. Samples were fixed in a homemade quartz cell equipped with KBr windows, allowing for measurement in a controlled atmosphere. Prior to the measurement, samples were activated at 150 °C in a dynamical vacuum. About 100 mbar (75 mmHg) of high-purity CO_2 was delivered into the cell.

Transmission electron microscopy (TEM) was performed on a FEI Tecnai G2 Spirit TWIN transmission electron microscope operated at an accelerating voltage of 80 kV. Sampling was done by the dispersion of powders in absolute ethanol. The average particle size was calculated as an arithmetic mean of a set of 50−100 values. Thermogravimetric analysis (TGA) was performed on a Jupiter STA 449 F5 analyzer (Netzsch) with samples held in corundum pans

DOI: 10.1021/acs.inorgchem.8b03087
Inorg. Chem. 2019, 58, 1607−1620

in a continuous nitrogen flow or in the flux of air with a heating rate of 10 °C/min.

2.3. Modeling. To estimate the binding energy between the H_2 molecule and the organic linkers used in the UiO-66 synthesis investigated in this work, we calculated the geometries and energies for the different configurations of the H_2 molecule adsorbed onto H_2BDC and H_2NDC linkers. The calculations were performed within the B3LYP density functional theory (DFT) level, as implemented in the *ADF-2017* program package.[70,71] The largest available quadruple-ζ with four polarization functions (QZ4P) basis set was used.[72] Among others, the hybrid B3LYP[73] exchange correlation functional with 20% exact Hartree−Fock exchange was used, which has recently shown its applicability to describe the H_2−C sp^2 interaction in the graphene sheet.[74] D3 dispersion correction was applied to account for van der Waals interactions.[75−77]

3. RESULTS AND DISCUSSION

3.1. Structural Analysis and Morphology. The results of laboratory PXRD characterization of the samples (Figure S1) testified to the good degree of crystallinity and phase purity of the obtained samples, confirming the UiO-66-like phase in all cases. A detailed structural analysis has been made on the synchrotron PXRD data reported in Figure 1a in the 2θ range of 4.5−10.5°. For the full range of patterns, see Figure S2. Of interest is the intensity inversion of the couples of reflections (311)−(222) and (331)−(420) by moving from 0NDC to 100NDC.

The refinement was made in the *Jana2006* program[67] (Figure S3). A spline background was subtracted from all of the patterns prior to the refinement to reduce the scattering contribution from the glass capillary. Three parameters of the pseudo-Voight function were used to describe the peak shape: GW, LX, and LY. The GW parameter was fixed to the value obtained for the LaB_6 standard. For the studied samples, the refined values of the Gaussian crystallite size-broadening parameter (GP) were negligibly small; therefore, GP was set to 0. The GU value for the LaB_6 refinement was negative and was also set to 0. The LX and LY parameters were used to calculate the crystal size and strain for the samples.

In the first refinement [performed in the space group $Fm\bar{3}m$ (No. 225)] of the 0NDC sample (i.e., UiO-66), the occupancy of the Zr atom was fixed to 1, and all other occupancies were optimized. The resulting values were 0.93, 0.87, 0.84, 0.89, and 0.86 for the O1, C11, C12, and C13 atoms, respectively (see Figure 1b for atom labeling). Therefore, in the following refinements, all occupancies for the C atoms and the O1 atom of the linker were constrained to be equal. The O2 position was split into O2A and O2B with equal occupancies, reflecting μ_3O and μ_3OH atoms in the middle of the eight triangular sides of the $Zr_6O_4(OH)_4$ SBU of UiO-66.[23,24] The distances between different pairs of neighboring C atoms were also set to be equal (C11−C12 = C12−C13). As reported in our previous work on pure UiO-66-NDC,[60] the contribution of C14 and C15 atoms to the electron density is relatively low because of their lower occupancy factor (taking into account the reduction due to symmetry) and the high anisotropic displacement due to the rotation of the linker. To refine all patterns with the same strategy, including the 25NDC and 50NDC ones, where the contribution of these atoms is even lower, we did not include the C14 and C15 atoms in the refinement procedure. This implies that the refined parameters for the 100NDC sample will be slightly different with respect to those published before, where all atoms of the NDC linker were refined.[60]

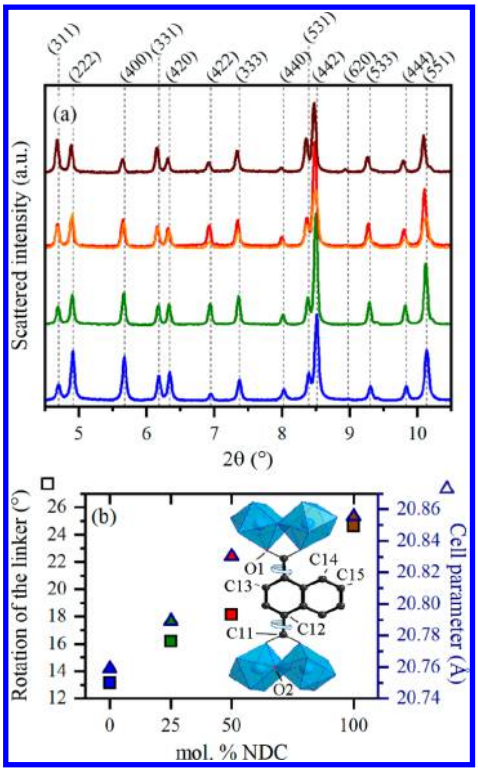

Figure 1. Part (a): Synchrotron radiation (λ = 0.51353) PXRD patterns of synthesized samples from bottom to top: 0NDC (blue), 25NDC (green), 50NDC (red) and 100NDC (brown), and mechanical mixture (orange) of 1:1 molar ratio of 0NDC and 100 NDC, superimposed on the 50NDC. Vertical dotted lines allow to appreciate the shift of the Bragg peaks (indexed on top) with increasing NDC content. Part (b): The dependence of the rotation angle of the average linkers (squares, left ordinate axis) and refined lattice parameter a (triangles, right ordinate axis) on the NDC content in the samples. Color designations as in part (a). The model in the bottom right corner of part (b) depicts connection of a linker with two SBU in the UiO-66-NDC structure. Blue polyhedra represent zirconium coordinated by oxygen ions, while the C atoms of the linker are represented by black spheres. Also reported are the labels used in the refinement to discriminate among crystallographic independent C and O atoms (atoms C14 and C15 are absent in BDC). The bent arrows indicate the C11−C12 rotational axis of the linker.

The C13 atom was moved from 96j to the less symmetric 192l site to allow rotation of the linker along the C11−C12 axis. We define as φ the rotation angle of the linkers, that is, the angle between the plane of the C atoms of the linker and the c−a direction (i.e., the dihedral angle between the O1−C11−C12 and C11−C12−C13 planes).

Table 1 reports the main results of the Rietveld analysis on four samples. With increasing NDC content, the lattice parameter a rises from 20.7589(1) to 20.8556(5) Å. The progressive increase of the lattice constant is related to the stress created by extra benzene rings of the NDC linker in comparison with the standard BDC ligands. Of interest is also the progressive increase of the tilting angle φ of the linkers with increasing NDC content, needed to avoid the steric hindrance of adjacent NDC linkers.[60]

To check that the intermediate synthesis resulted in a single phase containing both linkers in the same crystals instead of two separate phases of pure MOFs with BDC or NDC linkers, we compare the PXRD pattern of the 50NDC sample with that

DOI: 10.1021/acs.inorgchem.8b03087
Inorg. Chem. 2019, 58, 1607−1620

obtained on a mechanical mixture of 0NDC and 100NDC in a 1:1 molar ratio (red and orange curves, respectively, in Figures 1a and S2). Because of the significant difference in the lattice parameters between the 0NDC and 100NDC samples, the mechanical mixture resulted in an intrinsic broadening of the Bragg reflections, which progressively increases with increasing 2θ. This broadening is not observed in the 50NDC sample, implying that the linkers are mixed in each crystallite, resulting in a unique lattice parameter of intermediate value. We used the (333) reflection, which is well isolated, to quantify the phenomenon: the full width at half-maximum (fwhm) moves from 0.060° to 0.079° with an increase of 30% (Table 2). Using a higher index reflection, the difference would have been even larger.

Table 2. Summary of the Rietveld Refinements of Synchrotron PXRD Data[a]

sample	cell parameter (Å)	$\text{fwhm}_{(333)}$ (deg)	φ (deg)
0NDC	20.7589(1)	0.065	13
25NDC	20.7892(2)	0.058	16
50NDC	20.8301(2)	0.060	18
100NDC	20.8556(5)	0.061	31
MM	20.7979(3)	0.079	16

[a] φ is the angle between the plane of the C atoms of the linker and the $c-a$ direction (i.e., the dihedral angle between the O1−C11−C12 and C11−C12−C13 planes). MM = mechanical mixture of 0NDC and 100NDC (1:1 moles). The space group $Fm\bar{3}m$ (No. 225) was used in all cases.

Figure 2 reports, for the four samples with different NDC contents, representative TEM images showing that in all cases the crystals have an octahedral shape typical for the UiO-66 phase.[60,78−80]

3.2. Volumetric Analysis, H_2-Adsorption Properties, and Related DFT Calculations. The N_2-sorption isotherms (Figure S4) are all of type I (IUPAC classification),[81] which is typical for microporous materials. For the sake of analysis, their adsorption branches are shown in the logarithmic scale in Figure 3a; this allows one to better appreciate the low-pressure region. The linear scale and whole pressure range for both the adsorption and desorption branches are presented in Figure S4a. As can be seen from Figure 3a, the tracks of isotherms in the low-pressure region deviate significantly on passing from that of the 0NDC sample to those of the samples with the NDC linker. In more detail, the isotherm of 0NDC exhibits three steps at relative pressures P/P_0 near 4×10^{-6}, 3×10^{-4}, and 3×10^{-2}, in good agreement with the previously reported data.[82] All others have one step only, which progressively moves to lower P/P_0 with increasing NDC content: 4×10^{-4}, 2×10^{-5}, and 5×10^{-6}. A multistep adsorption isotherm was already observed in UiO-66[82,83] and other MOFs.[82,84,85] For ZIF-8 MOF, two possible explanations were proposed: (i) reorganization of adsorbed N_2 molecules in the pores;[84] (ii) an increase in the size of the pore windows after the threshold pressures were reached.[85] For UiO-66, the phenomenon was explained in terms of the successive filling of the octahedral and tetrahedral cages[82] or the gate-opening effect caused by pressure-induced linker tilt.[83] The latter hypothesis could explain the absence of the multistep adsorption isotherm in

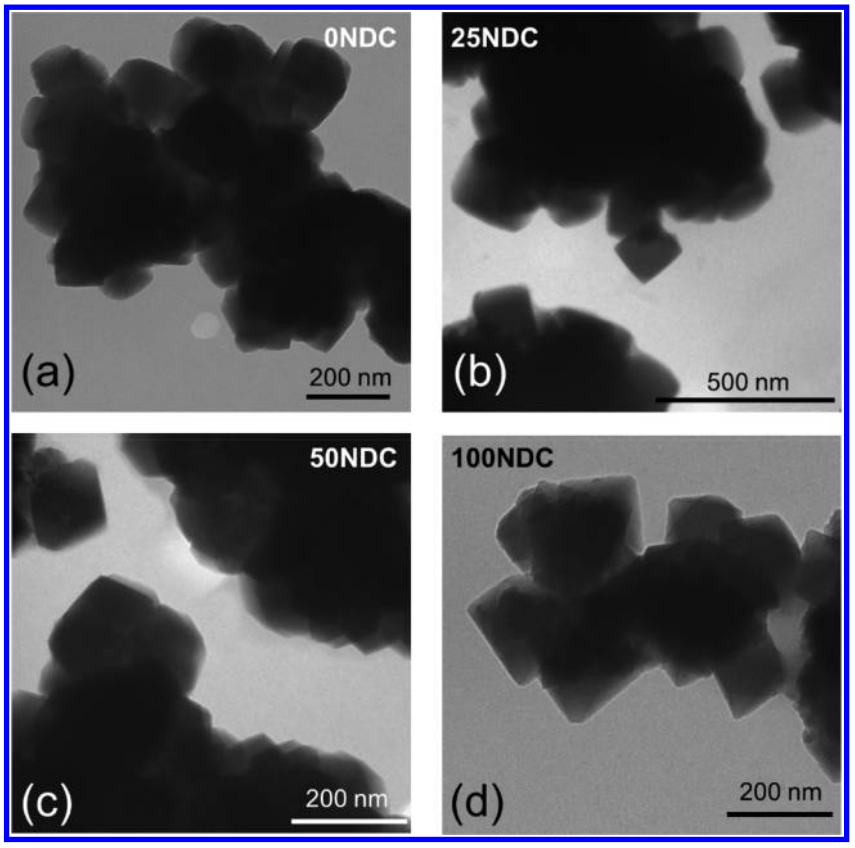

Figure 2. TEM images of samples with increasing NDC content.

DOI: 10.1021/acs.inorgchem.8b03087
Inorg. Chem. 2019, 58, 1607−1620

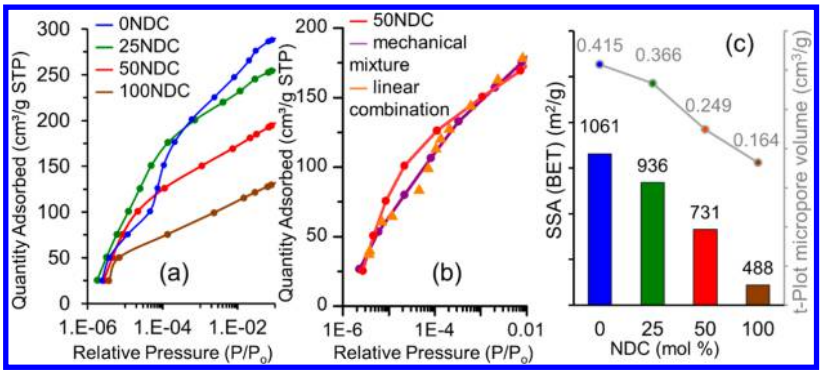

Figure 3. (a) Logarithmic plot (in the low-pressure region) of N_2 adsorption at 77 K on samples with different NDC contents. (b) Like part a for the 50NDC sample (red dots), compared with a mechanical mixture of 0NDC and 100NDC (1:1 in moles, purple dots) and with a linear combination (orange triangles) of the two isotherms collected on the MOFs synthesized with pure ligands (0NDC + 100NDC)/2 and reported in part a. (c) BET surface area (bar histogram, left ordinate axis) and micropore volume (colored dots, right ordinate axis) of samples with different NDC contents.

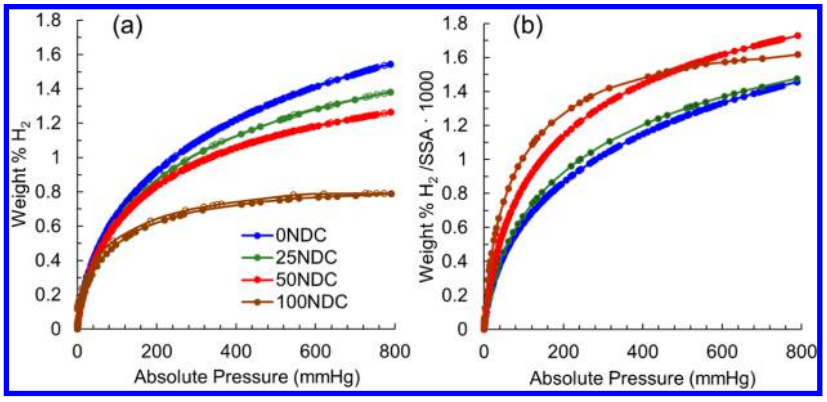

Figure 4. (a) H_2-adsorption (solid circles) and H_2-desorption (open circles) isotherms collected at 77 K for samples with different NDC contents. (b) Like part a, renormalized by the BET SSA of the different MOFs (Table 1). A similar result is obtained when normalization is made with the pore volume value (Figure S5).

Table 3. Relative Ranking of Samples with Different NDC Contents in the Amount of H_2 Adsorption in Different Pressure Ranges

	$P(H_2)$ (mmHg)				
	<5	5−11	11−14	14−30	>30
1st material	100NDC	0NDC	0NDC	0NDC	0NDC
2nd material	0NDC	100NDC	50NDC	50NDC	25NDC
3rd material	50NDC	50NDC	100NDC	25NDC	50NDC
4th material	25NDC	25NDC	25NDC	100NDC	100NDC

samples containing NDC linkers because they are already tilted in their equilibrium position.[60]

Moreover, we used the slope of the N_2 isotherms as a fingerprint to prove that the NDC and BDC linkers mix into a single phase, confirming the analogous comparison done with PXRD experiments (Figure 1a and Table 1). To this aim, we have compared the isotherms of a mechanical mixture of 0NDC and 100NDC samples with that of the 50NDC sample (Figure 3b in the low-pressure range; see Figure S4b for the whole range). The measured isotherm of the mechanical mixture (purple curve) is in good agreement with the mathematical average of the 0NDC and 100NDC isotherms (orange curves), while the 50NDC one differs from it and could not be obtained as a simple mathematic combination of the 0NDC and 100NDC isotherms in both low and high P/P_0 ranges. The BET SSA of the mechanical mixture is 771 m^2/g, a value that is in a good agreement with the average mean of the 0NDC and 100NDC surface areas (774 m^2/g) and that differs significantly from that of the 50NDC sample (732 m^2/g).

The SSA values were calculated by the BET method[68] and presented with respect to the NDC content in Figure 3c and Table 1. SSA (micropore volume) decreases from 1061 m^2/g (0.415 cm^3/g) to 488 m^2/g (0.164 cm^3/g) with an increase of the NDC fraction, which is expected because of occupation of the pore's space by the more bulky naphthalene rings. Finally, in the N_2 isotherms, we have observed a small hysteresis loop for the samples 50NDC and 100NDC (Figure S4a). In this regard, it is worth mentioning that similar hysteresis loops have been observed by Liu et al.[86] in HKUST-1.[87,88] The authors provided evidence for the formation of mesopores due to partial replacement of the BTC linkers by a second ligand (benzoic acid). We believe that a similar effect is also taking place in the present case of the mixed ligand UiO-66. This is a relevant point because the presence of mesopores in UiO-66

DOI: 10.1021/acs.inorgchem.8b03087
Inorg. Chem. 2019, 58, 1607−1620

can overcome the limitations of UiO-66 for many applications because of the restricted size of their micropores. The development of synthesis procedures aimed to create mesoporosity in MOFs is a highly investigated topic[86,89−92] because the presence of mesopores, resulting in hierarchical structures, represents a significant improvement of the MOF diffusion properties, especially when the mesoporosity can be controlled at will during synthesis.

H_2-adsorption isotherms are presented in Figure 4a. The H_2 uptake at high pressures decreases with an increase of the NDC content, in good agreement with the BET SSA values. This effect, however, does not hold for the whole pressure range; the relative ranking of the four materials changes with pressure, as reported in Table 3. Indeed, up to 5 mmHg, the H_2 uptake is larger for the 100NDC sample, and then with increasing pressure, the relative ranking of this material starts to progressively decline. This effect can be explained in terms of a slightly more efficient interaction between the H_2 molecule and the naphthalene rings, with respect to the benzene one and by the fact that there are two rings available for adsorption in the case of the NDC linker. There is a compromise between the presence of the NDC linker and the total surface area available in determining the ranking scale of the four materials: at low pressure, the former prevails, and at higher pressure, the latter dominates. At pressures larger than 30 mmHg, the ranking is uniquely driven by the SSA of the material.

If we normalize the H_2-adsorption isotherms of Figure 4a by the BET SSA value, we obtain the curves reported in Figure 4b, which clearly shows that the H_2 adsorption per unit of internal surface area is significantly higher for the 100NDC sample than for the 0NDC one, in the whole pressure range. A comparable result is obtained when normalization is made with the pore volume value, as reported in Figure S5.

Finally, we have observed very small hysteresis loops in samples 25NDC and 50NDC and more consistent in the 100NDC sample. The phenomenon is attributed to the retention of H_2 molecules by the naphthalene ring system.[93,94]

To support the experimental findings reported in Figure 4 and Table 3, we performed DFT calculations (see section 2.3) on H_2 adsorption for both the H_2BDC and H_2NDC linkers. The optimized geometries are reported in Figure 5, while relevant quantitative geometrical and energetical values are listed in Table 4. To simulate, in the first approximation, the constraints imposed by the insertion of the linkers inside the MOF framework, the positions of the four O atoms of the carboxylate units have been fixed to the crystallographic positions obtained in the XRD refinements performed on UiO-66[24] and on UiO-66-NDC[60] for the H_2BDC and H_2NDC linkers, respectively. On the H_2BDC linker, the side-on geometry (Figure 5a) is slightly preferred with respect to the end-on one (Figure 5b) by 0.291 kJ/mol and results in an adsorption distance of d_{H2-C6} = 2.97 Å, measured from the center of mass of the H_2 molecule and the plane of the six C atoms. The adsorption angle is slightly tilted by 5° with respect of the C-atom plane (Figure 5a). For the end-on configuration, the optimized geometry differs by more than 30° from the starting one. Adsorption of the H_2 molecule on the H_2NDC linker can occur either on the ring connected to the carboxylate units (ring R1, Figure 5c,e, side- and end-on geometries, respectively) or on the adjacent one (ring R2, Figure 5d,f, side- and end-on geometries, respectively). The DFT calculations show that for both side- and end-on configurations the presence of two adjacent sp^2-hybridized C

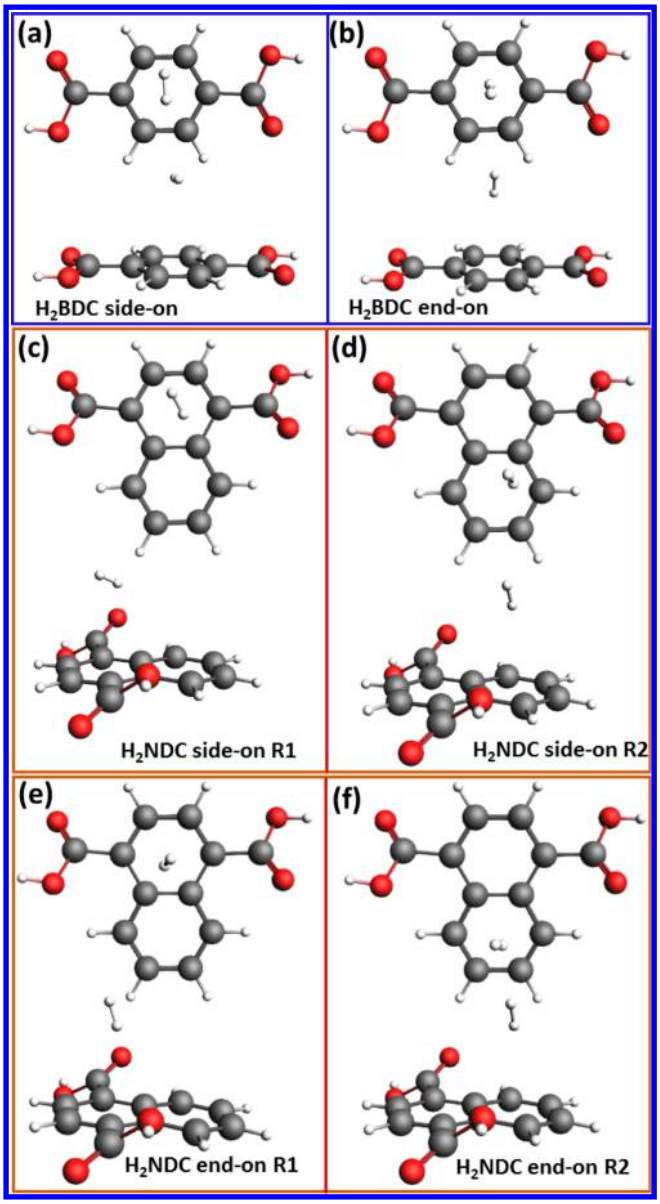

Figure 5. Optimized geometries for the adsorption of H_2 on the linkers: (a) side-on starting geometry on the H_2BDC linker; (b) end-on starting geometry on the H_2BDC linker; (c) side-on starting geometry on the H_2NDC linker, ring R1; (d) side-on starting geometry on the H_2NDC linker, ring R2; (e) end-on starting geometry on the H_2NDC linker, ring R1; (f) end-on starting geometry on the H_2NDC linker, ring R2.

rings slightly enhances the interaction energy of H_2 with the π orbitals of the aromatic ring. This holds for adsorptions on both the R1 and R2 rings of the H_2NDC linker (Table 3). Adsorption on the R2 ring results in two similarly optimized adducts (both structural and energetic grounds), while adsorption on R1 clearly favors the side-on geometry with an adsorption energy of 4.656 kJ/mol, an adsorption distance of d_{H2-C6} = 2.95 Å, a significantly tilted angle of 27° (Table 3 and Figure 5c). This geometry represents the more stable one for the H_2 molecule among the investigated ones and is energetically more favored than the best one for the H_2BDC linker by 15%. This computational study explains the experimental evidence that, at low equilibrium pressure, H_2 adsorption is more efficient in the 100NDC sample and that,

DOI: 10.1021/acs.inorgchem.8b03087
Inorg. Chem. 2019, 58, 1607−1620

Table 4. Summary of the DFT Study of H_2 Adsorbed on H_2BDC and H_2NDC[a]

linker	ads site	ads geometry	ΔE (meV)	ΔE (kJ/mol)	$\Delta E/E$ (%)	d_{H2-C6} (Å)	α (deg)
H_2BDC	R1	end-on	44.45	4.289	0	3.03	69
H_2BDC	R1	side-on	41.44	3.998	0	2.97	5
H_2NDC	R1	end-on	46.86	4.521	+5.4	3.00	68
H_2NDC	R1	side-on	48.25	4.656	+15.1	2.95	27
H_2NDC	R2	end-on	47.35	4.568	+6.5	3.04	69
H_2NDC	R2	side-on	47.68	4.600	+7.3	3.02	63

[a]R1 is the benzene ring connected via the carboxylates units to the MOF framework, and R2 is the adjacent one present in H_2NDC only. Both end- and side-on adsorption geometries were tried. Adsorption energies are reported in both millielectronvolts and kilojoules per mole. $\Delta E/E$ represents the percentage of increased adsorption energy observed for H_2 adsorption on H_2NDC with respect to that obtained for adsorption on H_2BDC with the same geometry. d_{H2-C6} is the distance between the center of mass of the H_2 molecule and the plane of the adsorption ring. α is the angle between the H_2 molecule axis and the plane of the adsorption ring: in the starting configuration, α = 0° and 90° for the side- and end-on configurations, respectively.

only at higher pressure, the adsorption ranking progressively favors samples with a higher internal available volume (Table 3).

3.3. Vibrational Properties: Framework Modes and CO_2 Adsorption. Vibrational spectroscopies represent a set of powerful characterization tools in understanding the MOF structure, composition, defectivity, reactivity, and surface properties.[23,32,38,88,95−113] The vibrational features of the whole set of samples is reported in parts a and b of Figure 6

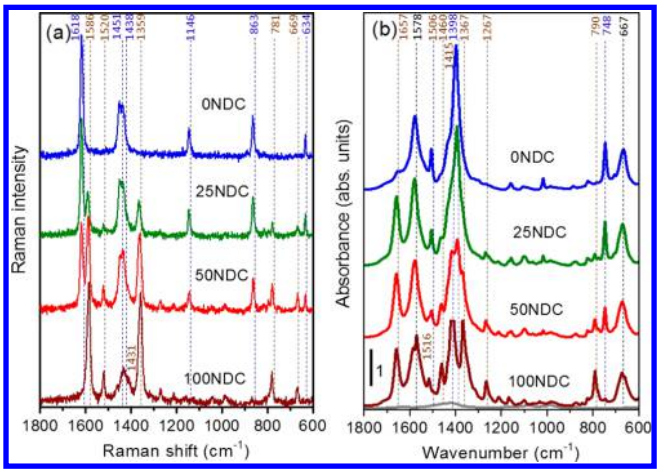

Figure 6. Vibrational study of samples with different NDC contents reported in the linkers *fingerprint* region. In both parts, the spectra are vertically shifted for clarity (increasing the NDC content from top to bottom). (a) Raman spectra obtained after subtraction of the fluorescence background. (b) FTIR spectra of samples diluted in KBr, the bare spectrum of which is reported as a gray curve in the bottom. Vertical dashed guidelines refer to the modes that are specific for BDC (blue) or NDC (brown) linkers. Linker-unspecific IR bands at 667 and 1578 cm^{-1} are highlighted with back vertical guidelines in part b. See Table 5 for the exact wavenumber of each mode and for the corresponding assignment.

for Raman and IR, respectively. From a structural point of view, both BDC and NDC have the same functional groups, implying a very similar vibrational profile. However, similar modes will occur at slightly different wavenumbers in the two linkers, allowing easy recognition of their spectral signature. The more relevant vibrational modes in both the Raman and IR spectra are listed in Table 5 (top and bottom parts, respectively), together with the corresponding assignment from the literature,[38,114,115] when available. The linker-specific bands are highlighted by vertical guidelines of blue and brown

Table 5. Summary of the Main Linker-Specific Vibrational Modes Observed in the Raman (Figure 6a) and IR (Figure 6b) Spectra Measured in This Work and Corresponding Assignments from the Literature, When Available (L n-s = Linker Nonspecific)

ν (cm^{-1})	linker	assignment	ref
		Raman Spectra	
634	BDC	benzene ring deformation in terephthalates	38
669	NDC	C−H out-of-plane symmetric bending	115
781	NDC	C−H out-of-plane asymmetric bending	115
863	BDC		
1146	BDC	terephthalate ring breathing + benzoate ring deformation	38
1359	NDC	C−C stretching + ring deformation	114
1431	NDC	C−C stretching + C−H bending	114
1438	BDC	OCO symmetric stretching in carboxylate in-phase	38
1451	BDC	OCO symmetric stretching in carboxylate in-phase	38
1520	NDC	in-plane ring deformation	115
1586	NDC	C═C stretching of aromatic rings	114
1618	BDC	C═C stretching of aromatic rings	38
		IR Spectra	
667	L n-s		
748	NDC	C−H wagging in-phase	114
791	BDC	C−H wagging in-phase	this work
1267	NDC	C−H bending out-of-phase and C−C stretching	114
1367	NDC	C−C stretching and C−H bending	114
1398	BDC	OCO symmetric stretching in carboxylate out-of-phase	38
1415	NDC	OCO symmetric stretching in carboxylate out-of-phase	this work
1460	NDC	C−C stretching and C−H bending	114
1506	BDC		
1516	NDC	C═C stretching	114
1578	L n-s	OCO asymmetric stretching in carboxylate	38
1657	NDC		
3672	L n-s	O−H stretching mode of unperturbed SBU μ_3OH	Figure 7a−d
3668	L n-s	O−H stretching mode of SBU μ_3OH perturbed by NDC	Figure 7b−d

color for the BDC and NDC linkers, respectively. Following the guidelines, when the NDC contents of the MOFs (from top to bottom in Figure 6) is increased, the increase of the NDC-specific bands and decrease of the BDC-specific ones are evident. This trend is, however, not perfectly linear with the

DOI: 10.1021/acs.inorgchem.8b03087
Inorg. Chem. 2019, 58, 1607−1620

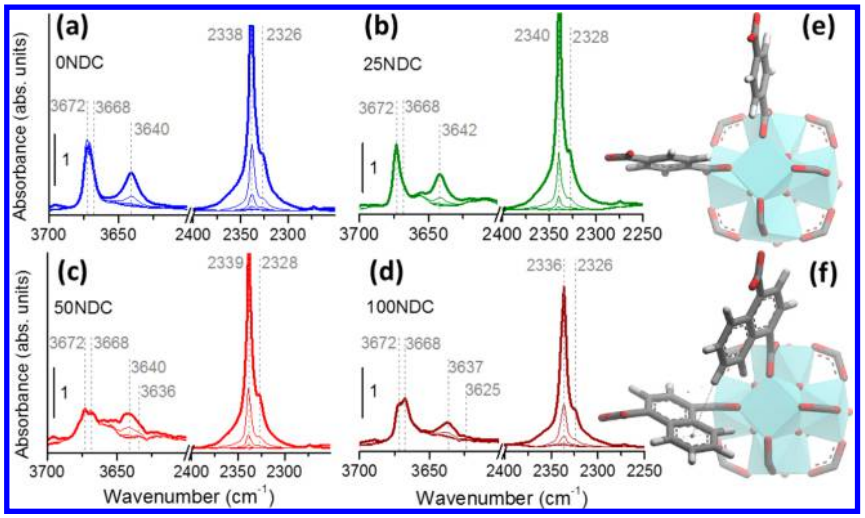

Figure 7. (a) FTIR spectra of CO_2 adsorption (at room temperature) on the 0NDC sample at different P_{CO_2} values (0, 0.3, 1, 3, 6, and 60 mbar). The left (3700−3600 cm^{-1}) and right (2400−2250 cm^{-1}) panels refer to the O−H stretching and CO_2 ν_3 stretching regions, respectively. (b−d) Like part a for the 25NDC, 50NDC, and 100NDC MOFs, respectively. (e) Graphical representation of the inorganic $Zr_6(OH)_4O_4$ SBU with two adjacent BDC linkers. The structure was taken from the single-crystal XRD refinement of 0NDC (UiO-66; $\varphi \sim 0°$).[24] (f) Like part e with two adjacent NDC linkers. The structure was taken from the PXRD refinement of 100NDC (UiO-66-NDC; $\varphi = 30°$).[60]

nominal NDC molar fraction, probably reflecting a slightly different incorporation fraction from the synthesis batch into the solid phase. The minor number of Raman-active modes makes the discrimination between the BDC and NDC bands more straightforward in the Raman spectra. IR bands are more convoluted, although the differences between the two extreme syntheses are also well-defined.

For the UiO-66 sample (0NDC), the most intense Raman band at 1618 cm^{-1} is attributed to the C═C aromatic stretch in the phase of the BDC linker, while the vibrational manifestation of the aromatic-ring in-plane bending is located at 634 cm^{-1} (Figure 6a).[38] These modes move to 1585 and 668 cm^{-1} in the Raman spectra of the 100NDC sample. The doublet peaking at 1452 and 1438 cm^{-1} is due to in-phase OCO symmetric stretching of the carboxylate group in the BDC linker,[38] which is replaced by a wide band peaking around 1431 cm^{-1} for the 100NDC sample, although this broad band is also visible at the foot of the doublet for all samples containing NDC.

To conclude with a description of the spectral profile of the 0NDC sample, we mention that the peak at 1146 cm^{-1} is due C−C symmetric ring breathing,[38] while that at 863 cm^{-1} is assigned to OH bending with some contribution from C−C symmetric breathing.[116] Instead, the 100NDC sample also contains bands at 1520 and 1359 cm^{-1} related to in-plane ring deformations and another one at 781 cm^{-1},[114,115] ascribed to out-of-plane asymmetric C−H bending.[115]

The FTIR spectra in Figure 6b show a complementary picture with a similar trend of the band appearance with respect to changing fractions of BDC/NDC linkers. The major features are the out-of-phase OCO symmetric stretching in carboxylate that occurs at 1398 cm^{-1} in 0NDC,[38] that moves to 1415 cm^{-1} in 100NDC; the in phase C−H wagging mode at 748 cm^{-1} that shifts to 790 cm^{-1} moving from 0NDC to 100NDC and a band at 1657 cm^{-1}, visible only when the NDC linker is present.

The urgent problem of reducing anthropogenic CO_2 emissions[117−120] has encouraged an impressive effort in investigating the potentialities of MOFs as porous materials for CO_2 capture.[121−133]

In this work, IR spectroscopy was used to follow CO_2 adsorption at room temperature as a function of increasing CO_2 equilibrium pressure (P_{CO_2}) on the samples with different NDC contents (Figure 7a−d; for each part, the left panel reports the O−H stretching region, while the right one reports the ν_3 stretching mode of the CO_2 molecule). In the gas phase, CO_2 is a linear triatomic molecule that exhibits three vibrational modes, usually defined as ν_1 (symmetric O═C═O stretching frequency, Raman active at 1388.3 cm^{-1}), ν_2 (doubly degenerate bending vibration, IR active at 667.3 cm^{-1}), and ν_3 (asymmetric O═C═O stretching frequency, IR active at 2349.3 cm^{-1}).[134] In our case, only the ν_3 region can be investigated because both ν_1 (IR active upon molecular adsorption) and ν_2 are obscured by strong framework modes of the UiO-66 framework.

Of interest is the O−H stretching region of the activated MOFs before CO_2 dosage: lowest curve in the left panels of parts a−d of Figure 7. The 0NDC sample exhibits the well-known sharp band at 3672 cm^{-1} due to the μ_3OH stretching mode of the unperturbed inorganic $Zr_6(OH)_4O_4$ SBU of UiO-66.[23,32,135] This band remains visible in all samples, but starting from 25NDC, a new component develops at 3668 cm^{-1}, first as a shoulder of the former band and then as the main component in that region (sample 100NDC). We attribute this new band at the μ_3OH stretching mode of the inorganic $Zr_6(OH)_4O_4$ SBU perturbed by the second ring of the NDC linker. Indeed, while the C−H terminals of the BDC linkers are far away from the μ_3OH groups of the SBU in UiO-66 (Figure 7e), they became much closer in the case for the NDC linkers. This allows the formation of a weak O···H bond between the H atom of the C−H group and the O atom of the μ_3OH groups (Figure 7f), with a consequent small awakening of the O−H bond reflected by a red shift of its stretching frequency by 4 cm^{-1}.

Coming to CO_2 adsorption, two ν_3 bands are observed at 2338 and 2327 cm^{-1} (±1 cm^{-1} in the four samples). The bands are red-shifted with respect to the CO_2 gas phase by 11

DOI: 10.1021/acs.inorgchem.8b03087
Inorg. Chem. 2019, 58, 1607−1620

and 22 cm^{-1}, respectively. The presence of two red-shifted components in the ν_3 mode of CO_2 adsorbed inside MOFs is quite common and already observed, e.g., for CPO-27-Ni (2341 and 2329 cm^{-1}),[98] HKUST-1 (2342 and 2333 cm^{-1}),[96] and MIL-100(Fe) (2344 and 2334 cm^{-1}).[103] This differs from that observed upon adsorption of CO_2 inside metal-alkali zeolites, where a single blue-shifted band was observed.[136,137] For a full quantitative understanding of the observed ν_3 frequencies, a DFT study is needed because the shift of the ν_3 mode cannot simply be correlated to the adsorption enthalpy of CO_2 on the specific site but is a complex combination of electron donation through the O atom and electron acceptance through the C atom of the CO_2 molecule;[138] such an investigation is, however, beyond the scope of the present work.

Of interest is the fact that μ_3OH bands (both 3672 and 3668 cm^{-1} components) are not affected by CO_2 adsorption, in none of the samples, meaning that CO_2 is not interacting with such groups at the temperature and pressures investigated in this work. Indeed, the broad absorption centered in the 3636–3632 cm^{-1} interval is not due to perturbed OH groups[139,140] but is the combination of ν_1 and ν_3 modes of adsorbed CO_2.[96,98] The very weak band around 2275 cm^{-1} is due to the natural ^{13}C abundance in CO_2.[96,98] Of relevance is also the absence of any band in the 2450–2380 cm^{-1}. Bands in this region were observed upon adsorption of CO_2 on exposed Cu^{2+} in HKUST-1 (2400 cm^{-1})[140] and on Ni^{2+} in CPO-27-Ni (2408 cm^{-1})[98] and alkali-metal exchanged M-ZSM-5 zeolites (on Li^+, Na^+, K^+, and Cs^+ at 2427, 2416, 2408, and 2400 cm^{-1}, respectively)[137] and attributed to a combination of ν_3 with a metal-framework vibration. The absence of such a band in the spectra reported in Figure 7a–d evidences the absence of the coordination vacancy on the Zr^{4+} centers in UiO-66 frameworks. Because of the relatively low extinction coefficient of such combination bands, we do not exclude a minor presence of defective sites in studied samples.

3.4. Thermal Stability. TGA curves of all samples (Figure 8a) revealed a first weight loss at the temperature below 100 °C, which is attributed to H_2O molecule evacuation from the pores. The TGA curve of the sample 0NDC has an additional small weight loss at 300 °C associated with DMF evacuation.[23,27,36,37] The temperature of decomposition of the obtained samples decreases with an increase of the NDC content from 530 °C (0NDC) to 480 °C (100NDC), as better evidenced in the first-derivative curves reported in Figure 8b (see Tables 1 and S1 for quantitative values).

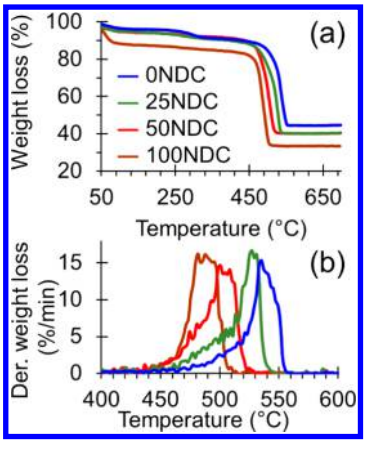

Figure 8. TGA thermograms (a) and first-derivative curves (b) of samples with different NDC contents.

4. CONCLUSIONS

We have successfully synthesized the set of UiO-66 MOFs with BDC/NDC mixed linkers: samples 0NDC (i.e., UiO-66), 25NDC, 50NDC, and 100NDC (i.e., UiO-66-NDC). Their structural, absorptive, and vibrational properties quantitatively correlate with the NDC content in the material. It is important to notice that the UiO-66 phase topology is preserved at all relative fractions of BDC/NDC. The comparison between synchrotron radiation PXRD and 77 K N_2-adsorption isotherms obtained on the 50NDC sample and on a mechanical mixture of 0NDC and 100NDC samples univocally proves that in sample 50NDC the BDC and NDC linkers are shared in each MOF crystal and discard the hypothesis of two independent phases, where each crystal contains only BDC or NDC linkers. The careful tuning of the NDC content opens a way for controlled alteration of the sorption properties of the resulting material, as testified by H_2-adsorption experiments showing that the relative rankings of the materials in the H_2 adsorption are different in different equilibrium pressure ranges: at low pressures, 100NDC is the most efficient sample, while with increasing pressure its relative performance progressively declines; at high pressures, the ranking follows the BDC content, reflecting the larger internal pore volume available in the MOFs with a higher fraction of smaller linkers. The H_2-adsorption isotherms normalized by the sample BET SSA show, in the whole pressure range, that the surface-area-specified H_2-adsorption capabilities in UiO-66 MOFs increase progressively with increasing NDC content. These results are supported by the DFT calculations. Finally, the presence of a significant hysteresis loop in the N_2-adsorption isotherm for the 50:50 BDC/NDC sample indicates the presence of mesopores, implying that hierarchical UiO-66 MOFs can be obtained by properly toning the linker ratio, with obvious improvement of the MOF diffusion properties.

■ ASSOCIATED CONTENT

Supporting Information

The Supporting Information is available free of charge on the ACS Publications website at DOI: 10.1021/acs.inorgchem.8b03087.

Laboratory PXRD patterns for all samples, synchrotron PXRD patterns for all samples (and for the mechanical mixture of a 1:1 molar ratio of 0NDC and 100NDC) in the full collected 2θ range, comparison between the observed and calculated (from Rietveld refinement) and difference PXRD profiles for the samples, N_2-adsorptiopn isotherms collected for all samples (and for the mechanical mixture of a 1:1 molar ratio of 0NDC and 100NDC) and reported in the whole pressure interval (linear scale), H_2-adsorption isotherms collected for samples normalized by the pore-volume values of the different MOFs, and quantitative details on the TGA experiments (PDF)

■ AUTHOR INFORMATION

Corresponding Authors

*E-mail: butovav86@gmail.com.
*E-mail: carlo.lamberti@unito.it.

DOI: 10.1021/acs.inorgchem.8b03087
Inorg. Chem. 2019, 58, 1607–1620

ORCID

Aram L. Bugaev: 0000-0001-8273-2560
Sachin M. Chavan: 0000-0002-9947-1018
Sigurd Øien-Ødegaard: 0000-0001-7913-4199
Carlo Lamberti: 0000-0001-8004-2312

Notes

The authors declare no competing financial interest.

■ ACKNOWLEDGMENTS

We are indebted to Silvia Bordiga for fruitful discussion. The Open Access Raman Laboratory at the NIS Interdepartmental Center of the Turin University is gratefully acknowledged. V.V.B. thanks Boris Bouchevreau for his support during her time at the Chemistry Department of the Oslo University. V.V.B., A.P.B., K.M.C., K.S.V.-N., A.L.B., A.A.G., A.V.S., and C.L. are thankful the support of the Mega-Grant of Ministry of Education and Science of the Russian Federation (Grant 14.Y26.31.0001). A.V.S., V.V.B., and K.S.V.-N. are thankful for the financial support of Russian Foundation for Basic Research to Research Project 18-29-04053. We are indebted to Vladimir Dmitriev, Herman Emerich, Wouter van Beek, and Michela Brunelli for their friendly and competent support during the experiment performed at the BM01B (now moved to BM31) beamline of the ESRF.

■ REFERENCES

(1) Li, J. R.; Kuppler, R. J.; Zhou, H. C. Selective gas adsorption and separation in metal-organic frameworks. *Chem. Soc. Rev.* **2009**, *38*, 1477−1504.
(2) Kuppler, R. J.; Timmons, D. J.; Fang, Q. R.; Li, J. R.; Makal, T. A.; Young, M. D.; Yuan, D. Q.; Zhao, D.; Zhuang, W. J.; Zhou, H. C. Potential applications of metal-organic frameworks. *Coord. Chem. Rev.* **2009**, *253*, 3042−3066.
(3) Czaja, A. U.; Trukhan, N.; Muller, U. Industrial applications of metal-organic frameworks. *Chem. Soc. Rev.* **2009**, *38*, 1284−1293.
(4) Ma, S. Q.; Zhou, H. C. Gas storage in porous metal-organic frameworks for clean energy applications. *Chem. Commun.* **2010**, *46*, 44−53.
(5) Corma, A.; Garcia, H.; Llabrés i Xamena, F. X. Engineering Metal Organic Frameworks for Heterogeneous Catalysis. *Chem. Rev.* **2010**, *110*, 4606−4655.
(6) Zhao, D.; Timmons, D. J.; Yuan, D. Q.; Zhou, H. C. Tuning the Topology and Functionality of Metal-Organic Frameworks by Ligand Design. *Acc. Chem. Res.* **2011**, *44*, 123−133.
(7) Li, J. R.; Sculley, J.; Zhou, H. C. Metal-Organic Frameworks for Separations. *Chem. Rev.* **2012**, *112*, 869−932.
(8) Zhou, H. C.; Long, J. R.; Yaghi, O. M. Introduction to Metal-Organic Frameworks. *Chem. Rev.* **2012**, *112*, 673−674.
(9) Gole, B.; Bar, A. K.; Mukherjee, P. S. Fluorescent metal-organic framework for selective sensing of nitroaromatic explosives. *Chem. Commun.* **2011**, *47*, 12137−12139.
(10) Furukawa, H.; Cordova, K. E.; O'Keeffe, M.; Yaghi, O. M. The Chemistry and Applications of Metal-Organic Frameworks. *Science* **2013**, *341*, 1230444.
(11) Llabres i Xamena, F. X.; Gascon, J. *Metal Organic Frameworks as Heterogeneous Catalysts*; Royal Society of Chemistry: Cambridge, U.K., 2013.
(12) Gole, B.; Bar, A. K.; Mukherjee, P. S. Modification of Extended Open Frameworks with Fluorescent Tags for Sensing Explosives: Competition between Size Selectivity and Electron Deficiency. *Chem. - Eur. J.* **2014**, *20*, 2276−2291.
(13) He, Y. B.; Zhou, W.; Qian, G. D.; Chen, B. L. Methane storage in metal-organic frameworks. *Chem. Soc. Rev.* **2014**, *43*, 5657−5678.
(14) Zhou, H. C.; Kitagawa, S. Metal-Organic Frameworks (MOFs). *Chem. Soc. Rev.* **2014**, *43*, 5415−5418.
(15) Gascon, J.; Corma, A.; Kapteijn, F.; Llabrés i Xamena, F. X. Metal Organic Framework Catalysis: Quo vadis? *ACS Catal.* **2014**, *4*, 361−378.
(16) Bosch, M.; Yuan, S.; Rutledge, W.; Zhou, H. C. Stepwise Synthesis of Metal-Organic Frameworks. *Acc. Chem. Res.* **2017**, *50*, 857−865.
(17) Rogge, S. M. J.; Bavykina, A.; Hajek, J.; Garcia, H.; Olivos-Suarez, A. I.; Sepulveda-Escribano, A.; Vimont, A.; Clet, G.; Bazin, P.; Kapteijn, F.; Daturi, M.; Ramos-Fernandez, E. V.; Llabrés i Xamena, F. X.; Van Speybroeck, V.; Gascon, J. Metal-organic and covalent organic frameworks as single-site catalysts. *Chem. Soc. Rev.* **2017**, *46*, 3134−3184.
(18) Butova, V. V.; Soldatov, M. A.; Guda, A. A.; Lomachenko, K. A.; Lamberti, C. Metal-Organic Frameworks: Structure, Properties, Synthesis, and Characterization. *Russ. Chem. Rev.* **2016**, *85*, 280−307.
(19) Gole, B.; Sanyal, U.; Banerjee, R.; Mukherjee, P. S. High Loading of Pd Nanoparticles by Interior Functionalization of MOFs for Heterogeneous Catalysis. *Inorg. Chem.* **2016**, *55*, 2345−2354.
(20) Yaghi, O. M.; O'Keeffe, M.; Ockwig, N. W.; Chae, H. K.; Eddaoudi, M.; Kim, J. Reticular synthesis and the design of new materials. *Nature* **2003**, *423*, 705−714.
(21) Tranchemontagne, D. J.; Mendoza-Cortes, J. L.; O'Keeffe, M.; Yaghi, O. M. Secondary building units, nets and bonding in the chemistry of metal-organic frameworks. *Chem. Soc. Rev.* **2009**, *38*, 1257−1283.
(22) Cavka, J. H.; Jakobsen, S.; Olsbye, U.; Guillou, N.; Lamberti, C.; Bordiga, S.; Lillerud, K. P. A new zirconium inorganic building brick forming metal organic frameworks with exceptional stability. *J. Am. Chem. Soc.* **2008**, *130*, 13850−13851.
(23) Valenzano, L.; Civalleri, B.; Chavan, S.; Bordiga, S.; Nilsen, M. H.; Jakobsen, S.; Lillerud, K. P.; Lamberti, C. Disclosing the Complex Structure of UiO-66 Metal Organic Framework: A Synergic Combination of Experiment and Theory. *Chem. Mater.* **2011**, *23*, 1700−1718.
(24) Øien, S.; Wragg, D.; Reinsch, H.; Svelle, S.; Bordiga, S.; Lamberti, C.; Lillerud, K. P. Detailed Structure Analysis of Atomic Positions and Defects in Zirconium Metal-Organic Frameworks. *Cryst. Growth Des.* **2014**, *14*, 5370−5372.
(25) Bai, Y.; Dou, Y. B.; Xie, L. H.; Rutledge, W.; Li, J. R.; Zhou, H. C. Zr-based metal-organic frameworks: design, synthesis, structure, and applications. *Chem. Soc. Rev.* **2016**, *45*, 2327−2367.
(26) Wu, H.; Chua, Y. S.; Krungleviciute, V.; Tyagi, M.; Chen, P.; Yildirim, T.; Zhou, W. Unusual and Highly Tunable Missing-Linker Defects in Zirconium Metal-Organic Framework UiO-66 and Their Important Effects on Gas Adsorption. *J. Am. Chem. Soc.* **2013**, *135*, 10525−10532.
(27) Shearer, G. C.; Chavan, S.; Ethiraj, J.; Vitillo, J. G.; Svelle, S.; Olsbye, U.; Lamberti, C.; Bordiga, S.; Lillerud, K. P. Tuned to Perfection: Ironing Out the Defects in Metal-Organic Framework UiO-66. *Chem. Mater.* **2014**, *26*, 4068−4071.
(28) Butova, V. V.; Budnyk, A. P.; Charykov, K. M.; Vetlitsyna-Novikova, K. S.; Lamberti, C.; Soldatov, A. V. Water as a structure-driving agent between the UiO-66 and MIL-140A metal−organic frameworks. *Chem. Commun.* **2019**, *55*, XX DOI: 10.1039/C8CC07709F.
(29) Kandiah, M.; Nilsen, M. H.; Usseglio, S.; Jakobsen, S.; Olsbye, U.; Tilset, M.; Larabi, C.; Quadrelli, E. A.; Bonino, F.; Lillerud, K. P. Synthesis and Stability of Tagged UiO-66 Zr-MOFs. *Chem. Mater.* **2010**, *22*, 6632−6640.
(30) Kandiah, M.; Usseglio, S.; Svelle, S.; Olsbye, U.; Lillerud, K. P.; Tilset, M. Post-synthetic modification of the metal-organic framework compound UiO-66. *J. Mater. Chem.* **2010**, *20*, 9848−9851.
(31) Garibay, S. J.; Cohen, S. M. Isoreticular synthesis and modification of frameworks with the UiO-66 topology. *Chem. Commun.* **2010**, *46*, 7700−7702.
(32) Chavan, S.; Vitillo, J. G.; Gianolio, D.; Zavorotynska, O.; Civalleri, B.; Jakobsen, S.; Nilsen, M. H.; Valenzano, L.; Lamberti, C.; Lillerud, K. P.; Bordiga, S. H_2 storage in isostructural UiO-67 and UiO-66 MOFs. *Phys. Chem. Chem. Phys.* **2012**, *14*, 1614−1626.

DOI: 10.1021/acs.inorgchem.8b03087
Inorg. Chem. 2019, 58, 1607−1620

(33) Ragon, F.; Campo, B.; Yang, Q.; Martineau, C.; Wiersum, A. D.; Lago, A.; Guillerm, V.; Hemsley, C.; Eubank, J. F.; Vishnuvarthan, M.; Taulelle, F.; Horcajada, P.; Vimont, A.; Llewellyn, P. L.; Daturi, M.; Devautour-Vinot, S.; Maurin, G.; Serre, C.; Devic, T.; Clet, G. Acid-functionalized UiO-66(Zr) MOFs and their evolution after intra-framework cross-linking: structural features and sorption properties. *J. Mater. Chem. A* **2015**, *3*, 3294−3309.
(34) Leus, K.; Perez, J. P. H.; Folens, K.; Meledina, M.; Van Tendeloo, G.; Du Laing, G.; Van Der Voort, P. UiO-66-$(SH)_2$ as stable, selective and regenerable adsorbent for the removal of mercury from water under environmentally-relevant conditions. *Faraday Discuss.* **2017**, *201*, 145−161.
(35) Vermoortele, F.; Bueken, B.; Le Bars, G.; Van de Voorde, B.; Vandichel, M.; Houthoofd, K.; Vimont, A.; Daturi, M.; Waroquier, M.; Van Speybroeck, V.; Kirschhock, C.; De Vos, D. E. Synthesis Modulation as a Tool To Increase the Catalytic Activity of Metal-Organic Frameworks: The Unique Case of UiO-66(Zr). *J. Am. Chem. Soc.* **2013**, *135*, 11465−11468.
(36) Shearer, G. C.; Vitillo, J. G.; Bordiga, S.; Svelle, S.; Olsbye, U.; Lillerud, K. P. Functionalizing the Defects: Postsynthetic Ligand Exchange in the Metal Organic Framework UiO-66. *Chem. Mater.* **2016**, *28*, 7190−7193.
(37) Shearer, G. C.; Chavan, S.; Bordiga, S.; Svelle, S.; Olsbye, U.; Lillerud, K. P. Defect Engineering: Tuning the Porosity and Composition of the Metal-Organic Framework UiO-66. *Chem. Mater.* **2016**, *28*, 3749−3761.
(38) Atzori, C.; Shearer, G. C.; Maschio, L.; Civalleri, B.; Bonino, F.; Lamberti, C.; Svelle, S.; Lillerud, K. P.; Bordiga, S. Effect of Benzoic Acid as a Modulator in the Structure of UiO-66: An Experimental and Computational Study. *J. Phys. Chem. C* **2017**, *121*, 9312−9324.
(39) Chavan, S. M.; Shearer, G. C.; Svelle, S.; Olsbye, U.; Bonino, F.; Ethiraj, J.; Lillerud, K. P.; Bordiga, S. Synthesis and Characterization of Amine-Functionalized Mixed-Ligand Metal-Organic Frameworks of UiO-66 Topology. *Inorg. Chem.* **2014**, *53*, 9509−9515.
(40) Øien, S.; Agostini, G.; Svelle, S.; Borfecchia, E.; Lomachenko, K. A.; Mino, L.; Gallo, E.; Bordiga, S.; Olsbye, U.; Lillerud, K. P.; Lamberti, C. Probing Reactive Platinum Sites in UiO-67 Zirconium Metal-Organic Frameworks. *Chem. Mater.* **2015**, *27*, 1042−1056.
(41) Braglia, L.; Borfecchia, E.; Maddalena, L.; Oien, S.; Lomachenko, K. A.; Bugaev, A. L.; Bordiga, S.; Soldatov, A. V.; Lillerud, K. P.; Lamberti, C. Exploring structure and reactivity of Cu sites in functionalized UiO-67 MOFs. *Catal. Today* **2017**, *283*, 89−103.
(42) Braglia, L.; Borfecchia, E.; Lomachenko, K. A.; Bugaev, A. L.; Guda, A. A.; Soldatov, A. V.; Bleken, B. T. L.; Oien-Odegaard, S.; Olsbye, U.; Lillerud, K. P.; Bordiga, S.; Agostini, G.; Manzoli, M.; Lamberti, C. Tuning Pt and Cu sites population inside functionalized UiO-67 MOF by controlling activation conditions. *Faraday Discuss.* **2017**, *201*, 265−286.
(43) Braglia, L.; Borfecchia, E.; Martini, A.; Bugaev, A. L.; Soldatov, A. V.; Oien-Odegaard, S.; Lonstad-Bleken, B. T.; Olsbye, U.; Lillerud, K. P.; Lomachenko, K. A.; Agostini, G.; Manzoli, M.; Lamberti, C. The duality of UiO-67-Pt MOFs: connecting treatment conditions and encapsulated Pt species by *operando* XAS. *Phys. Chem. Chem. Phys.* **2017**, *19*, 27489−27507.
(44) Gonzalez, M. I.; Oktawiec, J.; Long, J. R. Ethylene oligomerization in metal-organic frameworks bearing nickel(II) 2,2'-bipyridine complexes. *Faraday Discuss.* **2017**, *201*, 351−367.
(45) Gutterod, E. S.; Oien-Odegaard, S.; Bossers, K.; Nieuwelink, A. E.; Manzoli, M.; Braglia, L.; Lazzarini, A.; Borfecchia, E.; Ahmadigoltapeh, S.; Bouchevreau, B.; Lonstad-Bleken, B. T.; Henry, R.; Lamberti, C.; Bordiga, S.; Weckhuysen, B. M.; Lillerud, K. P.; Olsbye, U. CO_2 Hydrogenation over Pt-Containing UiO-67 Zr-MOFs-The Base Case. *Ind. Eng. Chem. Res.* **2017**, *56*, 13206−13219.
(46) Bugaev, A. L.; Guda, A. A.; Lomachenko, K. A.; Kamyshova, E. G.; Soldatov, M. A.; Kaur, G.; Oien-Odegaard, S.; Braglia, L.; Lazzarini, A.; Manzoli, M.; Bordiga, S.; Olsbye, U.; Lillerud, K. P.; Soldatov, A. V.; Lamberti, C. Operando study of palladium nanoparticles inside UiO-67 MOF for catalytic hydrogenation of hydrocarbons. *Faraday Discuss.* **2018**, *208*, 287−306.
(47) Jakobsen, S.; Gianolio, D.; Wragg, D. S.; Nilsen, M. H.; Emerich, H.; Bordiga, S.; Lamberti, C.; Olsbye, U.; Tilset, M.; Lillerud, K. P. Structural determination of a highly stable metal-organic framework with possible application to interim radioactive waste scavenging: Hf-UiO-66. *Phys. Rev. B: Condens. Matter Mater. Phys.* **2012**, *86*, No. 125429.
(48) deKrafft, K. E.; Boyle, W. S.; Burk, L. M.; Zhou, O. Z.; Lin, W. B. Zr- and Hf-based nanoscale metal-organic frameworks as contrast agents for computed tomography. *J. Mater. Chem.* **2012**, *22*, 18139−18144.
(49) Waitschat, S.; Frohlich, D.; Reinsch, H.; Terraschke, H.; Lomachenko, K. A.; Lamberti, C.; Kummer, H.; Helling, T.; Baumgartner, M.; Henninger, S.; Stock, N. Synthesis of M-UiO-66 (M = Zr, Ce or Hf) employing 2,5-pyridinedicarboxylic acid as a linker: defect chemistry, framework hydrophilisation and sorption properties. *Dalton Trans.* **2018**, *47*, 1062−1070.
(50) Nouar, F.; Breeze, M. I.; Campo, B. C.; Vimont, A.; Clet, G.; Daturi, M.; Devic, T.; Walton, R. I.; Serre, C. Tuning the properties of the UiO-66 metal organic framework by Ce substitution. *Chem. Commun.* **2015**, *51*, 14458−14461.
(51) Lammert, M.; Wharmby, M. T.; Smolders, S.; Bueken, B.; Lieb, A.; Lomachenko, K. A.; De Vos, D.; Stock, N. Cerium-based metal organic frameworks with UiO-66 architecture: synthesis, properties and redox catalytic activity. *Chem. Commun.* **2015**, *51*, 12578−12581.
(52) Smolders, S.; Lomachenko, K. A.; Bueken, B.; Struyf, A.; Bugaev, A. L.; Atzori, C.; Stock, N.; Lamberti, C.; Roeffaers, M. B. J.; De Vos, D. E. Unravelling the Redox-catalytic Behavior of Ce^{4+} Metal-Organic Frameworks by X-ray Absorption Spectroscopy. *ChemPhysChem* **2018**, *19*, 373−378.
(53) Lomachenko, K. A.; Jacobsen, J.; Bugaev, A. L.; Atzori, C.; Bonino, F.; Bordiga, S.; Stock, N.; Lamberti, C. Exact Stoichiometry of Ce_xZr_{6-x} Cornerstones in Mixed-Metal UiO-66 Metal−Organic Frameworks Revealed by Extended X-ray Absorption Fine Structure Spectroscopy. *J. Am. Chem. Soc.* **2018**, *140*, 17379.
(54) Kim, M.; Cahill, J. F.; Fei, H. H.; Prather, K. A.; Cohen, S. M. Postsynthetic Ligand and Cation Exchange in Robust Metal-Organic Frameworks. *J. Am. Chem. Soc.* **2012**, *134*, 18082−18088.
(55) Hon Lau, C. H.; Babarao, R.; Hill, M. R. A route to drastic increase of CO_2 uptake in Zr metal organic framework UiO-66. *Chem. Commun.* **2013**, *49*, 3634−3636.
(56) Lee, Y.; Kim, S.; Kang, J. K.; Cohen, S. M. Photocatalytic CO_2 reduction by a mixed metal (Zr/Ti), mixed ligand metal-organic framework under visible light irradiation. *Chem. Commun.* **2015**, *51*, 5735−5738.
(57) Smith, S. J. D.; Ladewig, B. P.; Hill, A. J.; Lau, C. H.; Hill, M. R. Post-synthetic Ti Exchanged UiO-66 Metal-Organic Frameworks that Deliver Exceptional Gas Permeability in Mixed Matrix Membranes. *Sci. Rep.* **2015**, *5*, 6.
(58) Santiago Portillo, A.; Baldovi, H. G.; García Fernandez, M. T.; Navalon, S.; Atienzar, P.; Ferrer, B.; Alvaro, M.; Garcia, H.; Li, Z. H. Ti as Mediator in the Photoinduced Electron Transfer of Mixed-Metal NH_2-UiO-66(Zr/Ti): Transient Absorption Spectroscopy Study and Application in Photovoltaic Cell. *J. Phys. Chem. C* **2017**, *121*, 7015−7024.
(59) Yuan, S.; Chen, Y. P.; Qin, J. S.; Lu, W. G.; Wang, X.; Zhang, Q.; Bosch, M.; Liu, T. F.; Lian, X. Z.; Zhou, H. C. Cooperative Cluster Metalation and Ligand Migration in Zirconium Metal-Organic Frameworks. *Angew. Chem., Int. Ed.* **2015**, *54*, 14696−14700.
(60) Butova, V. V.; Budnyk, A. P.; Guda, A. A.; Lomachenko, K. A.; Bugaev, A. L.; Soldatov, A. V.; Chavan, S. M.; Oien-Odegaard, S.; Olsbye, U.; Lillerud, K. P.; Atzori, C.; Bordiga, S.; Lamberti, C. Modulator effect in UiO-66-NDC (1,4-naphthalenedicarboxilic acid) synthesis and comparison with UiO-67-NDC isoreticular MOFs. *Cryst. Growth Des.* **2017**, *17*, 5422−5431.
(61) Kleist, W.; Jutz, F.; Maciejewski, M.; Baiker, A. Mixed-Linker Metal-Organic Frameworks as Catalysts for the Synthesis of

DOI: 10.1021/acs.inorgchem.8b03087
Inorg. Chem. 2019, 58, 1607−1620

Propylene Carbonate from Propylene Oxide and CO_2. *Eur. J. Inorg. Chem.* **2009**, *2009*, 3552−3561.
(62) Deng, H. X.; Doonan, C. J.; Furukawa, H.; Ferreira, R. B.; Towne, J.; Knobler, C. B.; Wang, B.; Yaghi, O. M. Multiple Functional Groups of Varying Ratios in Metal-Organic Frameworks. *Science* **2010**, *327*, 846−850.
(63) Kleist, W.; Maciejewski, M.; Baiker, A. MOF-5 based mixed-linker metal-organic frameworks: Synthesis, thermal stability and catalytic application. *Thermochim. Acta* **2010**, *499*, 71−78.
(64) Marx, S.; Kleist, W.; Baiker, A. Synthesis, structural properties, and catalytic behavior of Cu-BTC and mixed-linker Cu-BTC-PyDC in the oxidation of benzene derivatives. *J. Catal.* **2011**, *281*, 76−87.
(65) van Beek, W.; Safonova, O. V.; Wiker, G.; Emerich, H. SNBL, a dedicated beamline for combinedin situ X-ray diffraction, X-ray absorption and Raman scattering experiments. *Phase Transitions* **2011**, *84*, 726−732.
(66) Knudsen, E. B.; Sorensen, H. O.; Wright, J. P.; Goret, G.; Kieffer, J. FabIO: easy access to two-dimensional X-ray detector images in Python. *J. Appl. Crystallogr.* **2013**, *46*, 537−539.
(67) Petříček, V.; Dušek, M.; Palatinus, L. Crystallographic Computing System JANA2006: General features. *Z. Kristallogr. - Cryst. Mater.* **2014**, *229*, 345−352.
(68) Brunauer, S.; Emmett, P. H.; Teller, E. Adsorption of Gases in Multimolecular Layers. *J. Am. Chem. Soc.* **1938**, *60*, 309−319.
(69) Barrett, E. P.; Joyner, L. G.; Halenda, P. P. The Determination of Pore Volume and Area Distributions in Porous Substances. I. Computations from Nitrogen Isotherms. *J. Am. Chem. Soc.* **1951**, *73*, 373−380.
(70) Fonseca Guerra, C.; Snijders, J. G.; te Velde, G.; Baerends, E. J. Towards an order-N DFT method. *Theor. Chem. Acc.* **1998**, *99*, 391−403.
(71) te Velde, G.; Bickelhaupt, F. M.; Baerends, E. J.; Fonseca Guerra, C.; Van Gisbergen, S. J. A.; Snijders, J. G.; Ziegler, T. Chemistry with ADF. *J. Comput. Chem.* **2001**, *22*, 931−967.
(72) Van Lenthe, E.; Baerends, E. J. Optimized slater-type basis sets for the elements 1−118. *J. Comput. Chem.* **2003**, *24*, 1142−1156.
(73) Reiher, M.; Salomon, O.; Artur Hess, B. Reparameterization of hybrid functionals based on energy differences of states of different multiplicity. *Theor. Chem. Acc.* **2001**, *107*, 48−55.
(74) Darvish Ganji, M.; Hosseini-khah, S. M.; Amini-tabar, Z. Theoretical insight into hydrogen adsorption onto graphene: a first-principles B3LYP-D3 study. *Phys. Chem. Chem. Phys.* **2015**, *17*, 2504−2511.
(75) Grimme, S.; Antony, J.; Ehrlich, S.; Krieg, H. A consistent and accurate ab initio parametrization of density functional dispersion correction (DFT-D) for the 94 elements H-Pu. *J. Chem. Phys.* **2010**, *132*, 154104.
(76) Grimme, S.; Hansen, A.; Brandenburg, J. G.; Bannwarth, C. Dispersion-Corrected Mean-Field Electronic Structure Methods. *Chem. Rev.* **2016**, *116*, 5105−5154.
(77) Smith, D. G. A.; Burns, L. A.; Patkowski, K.; Sherrill, C. D. Revised Damping Parameters for the D3 Dispersion Correction to Density Functional Theory. *J. Phys. Chem. Lett.* **2016**, *7*, 2197−2203.
(78) Zhao, Q.; Yuan, W.; Liang, J. M.; Li, J. P. Synthesis and hydrogen storage studies of metal-organic framework UiO-66. *Int. J. Hydrogen Energy* **2013**, *38*, 13104−13109.
(79) Miao, Y. R.; Su, Z.; Suslick, K. S. Energy Storage during Compression of Metal-Organic Frameworks. *J. Am. Chem. Soc.* **2017**, *139*, 4667−4670.
(80) Sava Gallis, D. F.; Harvey, J. A.; Pearce, C. J.; Hall, M. G.; DeCoste, J. B.; Kinnan, M. K.; Greathouse, J. A. Efficient MOF-based degradation of organophosphorus compounds in non-aqueous environments. *J. Mater. Chem. A* **2018**, *6*, 3038−3045.
(81) Sing, K. S. W.; Everett, D. H.; Haul, R. A. W.; Moscou, L.; Pierotti, R. A.; Rouquerol, J.; Siemieniewska, T. Reporting physisorption data for gas solid systems with special reference to the determination of surface-area and porosity (Recommendations 1984). *Pure Appl. Chem.* **1985**, *57*, 603−619.
(82) Chung, J. Y.; Liao, C. W.; Chang, Y. W.; Chang, B. K.; Wang, H.; Li, J.; Wang, C. Y. Influence of Metal-Organic Framework Porosity on Hydrogen Generation from Nanoconfined Ammonia Borane. *J. Phys. Chem. C* **2017**, *121*, 27369−27378.
(83) Friebe, S.; Geppert, B.; Steinbach, F.; Caro, J. Metal-Organic Framework UiO-66 Layer: A Highly Oriented Membrane with Good Selectivity and Hydrogen Permeance. *ACS Appl. Mater. Interfaces* **2017**, *9*, 12878−12885.
(84) Park, K. S.; Ni, Z.; Cote, A. P.; Choi, J. Y.; Huang, R. D.; Uribe-Romo, F. J.; Chae, H. K.; O'Keeffe, M.; Yaghi, O. M. Exceptional chemical and thermal stability of zeolitic imidazolate frameworks. *Proc. Natl. Acad. Sci. U. S. A.* **2006**, *103*, 10186−10191.
(85) Fairen-Jimenez, D.; Moggach, S. A.; Wharmby, M. T.; Wright, P. A.; Parsons, S.; Duren, T. Opening the Gate: Framework Flexibility in ZIF-8 Explored by Experiments and Simulations. *J. Am. Chem. Soc.* **2011**, *133*, 8900−8902.
(86) Liu, B. Y.; Li, Y. Y.; Oh, S. C.; Fang, Y. X.; Xi, H. X. Fabrication of a hierarchically structured HKUST-1 by a mixed-ligand approach. *RSC Adv.* **2016**, *6*, 61006−61012.
(87) Chui, S. S. Y.; Lo, S. M. F.; Charmant, J. P. H.; Orpen, A. G.; Williams, I. D. A chemically functionalizable nanoporous material $[Cu_3(TMA)_2(H_2O)_3]_n$. *Science* **1999**, *283*, 1148−1150.
(88) Prestipino, C.; Regli, L.; Vitillo, J. G.; Bonino, F.; Damin, A.; Lamberti, C.; Zecchina, A.; Solari, P. L.; Kongshaug, K. O.; Bordiga, S. Local structure of framework Cu(II) in HKUST-1 metallorganic framework: Spectroscopic characterization upon activation and interaction with adsorbates. *Chem. Mater.* **2006**, *18*, 1337−1346.
(89) Sudik, A. C.; Cote, A. P.; Wong-Foy, A. G.; O'Keeffe, M.; Yaghi, O. M. A metal-organic framework with a hierarchical system of pores and tetrahedral building blocks. *Angew. Chem., Int. Ed.* **2006**, *45*, 2528−2533.
(90) Qiu, L. G.; Xu, T.; Li, Z. Q.; Wang, W.; Wu, Y.; Jiang, X.; Tian, X. Y.; Zhang, L. D. Hierarchically Micro- and Mesoporous Metal-Organic Frameworks with Tunable Porosity. *Angew. Chem., Int. Ed.* **2008**, *47*, 9487−9491.
(91) Bradshaw, D.; El-Hankari, S.; Lupica-Spagnolo, L. Supramolecular templating of hierarchically porous metal-organic frameworks. *Chem. Soc. Rev.* **2014**, *43*, 5431−5443.
(92) Fang, Z. L.; Durholt, J. P.; Kauer, M.; Zhang, W. H.; Lochenie, C.; Jee, B.; Albada, B.; Metzler-Nolte, N.; Poppl, A.; Weber, B.; Muhler, M.; Wang, Y. M.; Schmid, R.; Fischer, R. A. Structural Complexity in Metal-Organic Frameworks: Simultaneous Modification of Open Metal Sites and Hierarchical Porosity by Systematic Doping with Defective Linkers. *J. Am. Chem. Soc.* **2014**, *136*, 9627−9636.
(93) Lin, X.; Telepeni, I.; Blake, A. J.; Dailly, A.; Brown, C. M.; Simmons, J. M.; Zoppi, M.; Walker, G. S.; Thomas, K. M.; Mays, T. J.; Hubberstey, P.; Champness, N. R.; Schroder, M. High Capacity Hydrogen Adsorption in Cu(II) Tetracarboxylate Framework Materials: The Role of Pore Size, Ligand Functionalization, and Exposed Metal Sites. *J. Am. Chem. Soc.* **2009**, *131*, 2159−2171.
(94) Yang, S. H.; Lin, X.; Dailly, A.; Blake, A. J.; Hubberstey, P.; Champness, N. R.; Schroder, M. Enhancement of H_2 Adsorption in Coordination Framework Materials by Use of Ligand Curvature. *Chem. - Eur. J.* **2009**, *15*, 4829−4835.
(95) Szeto, K. C.; Lillerud, K. P.; Tilset, M.; Bjorgen, M.; Prestipino, C.; Zecchina, A.; Lamberti, C.; Bordiga, S. A thermally stable Pt/Y-based metal-organic framework: Exploring the accessibility of the metal Centers with spectroscopic methods using H_2O, CH_3OH, and CH_3CN as probes. *J. Phys. Chem. B* **2006**, *110*, 21509−21520.
(96) Bordiga, S.; Regli, L.; Bonino, F.; Groppo, E.; Lamberti, C.; Xiao, B.; Wheatley, P. S.; Morris, R. E.; Zecchina, A. Adsorption properties of HKUST-1 toward hydrogen and other small molecules monitored by IR. *Phys. Chem. Chem. Phys.* **2007**, *9*, 2676−2685.
(97) Szeto, K. C.; Prestipino, C.; Lamberti, C.; Zecchina, A.; Bordiga, S.; Bjorgen, M.; Tilset, M.; Lillerud, K. P. Characterization of a new porous Pt-containing metal-organic framework containing potentially catalytically active sites: Local electronic structure at the metal centers. *Chem. Mater.* **2007**, *19*, 211−220.

DOI: 10.1021/acs.inorgchem.8b03087
Inorg. Chem. 2019, 58, 1607−1620

(98) Dietzel, P. D. C.; Johnsen, R. E.; Fjellvag, H.; Bordiga, S.; Groppo, E.; Chavan, S.; Blom, R. Adsorption properties and structure of CO_2 adsorbed on open coordination sites of metal-organic framework Ni_2(dhtp) from gas adsorption, IR spectroscopy and X-ray diffraction. *Chem. Commun.* **2008**, 5125−5127.
(99) Bonino, F.; Chavan, S.; Vitillo, J. G.; Groppo, E.; Agostini, G.; Lamberti, C.; Dietzel, P. D. C.; Prestipino, C.; Bordiga, S. Local structure of CPO-27-Ni metallorganic framework upon dehydration and coordination of NO. *Chem. Mater.* **2008**, *20*, 4957−4968.
(100) Chavan, S.; Vitillo, J. G.; Groppo, E.; Bonino, F.; Lamberti, C.; Dietzel, P. D. C.; Bordiga, S. CO Adsorption on CPO-27-Ni Coordination Polymer: Spectroscopic Features and Interaction Energy. *J. Phys. Chem. C* **2009**, *113*, 3292−3299.
(101) Lamberti, C.; Zecchina, A.; Groppo, E.; Bordiga, S. Probing the surfaces of heterogeneous catalysts by in situ IR spectroscopy. *Chem. Soc. Rev.* **2010**, *39*, 4951−5001.
(102) Vimont, A.; Thibault-Starzyk, F.; Daturi, M. Analysing and understanding the active site by IR spectroscopy. *Chem. Soc. Rev.* **2010**, *39*, 4928−4950.
(103) Leclerc, H.; Vimont, A.; Lavalley, J. C.; Daturi, M.; Wiersum, A. D.; Llwellyn, P. L.; Horcajada, P.; Ferey, G.; Serre, C. Infrared study of the influence of reducible iron(III) metal sites on the adsorption of CO, CO_2, propane, propene and propyne in the mesoporous metal-organic framework MIL-100. *Phys. Chem. Chem. Phys.* **2011**, *13*, 11748−11756.
(104) Wuttke, S.; Bazin, P.; Vimont, A.; Serre, C.; Seo, Y. K.; Hwang, Y. K.; Chang, J. S.; Ferey, G.; Daturi, M. Discovering the Active Sites for C3 Separation in MIL-100(Fe) by Using Operando IR Spectroscopy. *Chem. - Eur. J.* **2012**, *18*, 11959−11967.
(105) Chavan, S.; Vitillo, J. G.; Uddin, M. J.; Bonino, F.; Lamberti, C.; Groppo, E.; Lillerud, K. P.; Bordiga, S. Functionalization of UiO-66 Metal-Organic Framework and Highly Cross-Linked Polystyrene with $Cr(CO)_3$: In Situ Formation, Stability, and Photoreactivity. *Chem. Mater.* **2010**, *22*, 4602−4611.
(106) Borfecchia, E.; Maurelli, S.; Gianolio, D.; Groppo, E.; Chiesa, M.; Bonino, F.; Lamberti, C. Insights into Adsorption of NH_3 on HKUST-1 Metal-Organic Framework: A Multitechnique Approach. *J. Phys. Chem. C* **2012**, *116*, 19839−19850.
(107) Valenzano, L.; Vitillo, J. G.; Chavan, S.; Civalleri, B.; Bonino, F.; Bordiga, S.; Lamberti, C. Structure-activity relationships of simple molecules adsorbed on CPO-27-Ni metal-organic framework: In situ experiments vs. theory. *Catal. Today* **2012**, *182*, 67−79.
(108) Bonino, F.; Lamberti, C.; Chavan, S.; Vitillo, J. G.; Bordiga, S., Characterization of MOFs. 1. Combined Vibrational and Electronic Spectroscopies. In *Metal Organic Frameworks as Heterogeneous Catalysts*; Xamena, F., Gascon, J., Eds.; Royal Society of Chemistry: Cambridge, U.K., 2013; pp 76−142.
(109) Chavan, S.; Bonino, F.; Valenzano, L.; Civalleri, B.; Lamberti, C.; Acerbi, N.; Cavka, J. H.; Leistner, M.; Bordiga, S. Fundamental Aspects of H_2S Adsorption on CPO-27-Ni. *J. Phys. Chem. C* **2013**, *117*, 15615−15622.
(110) Chavan, S. M.; Zavorotynska, O.; Lamberti, C.; Bordiga, S. H_2 interaction with divalent cations in isostructural MOFs: a key study for variable temperature infrared spectroscopy. *Dalton Trans.* **2013**, *42*, 12586−12595.
(111) Wee, L. H.; Bonino, F.; Lamberti, C.; Bordiga, S.; Martens, J. A. Cr-MIL-101 encapsulated Keggin phosphotungstic acid as active nanomaterial for catalysing the alcoholysis of styrene oxide. *Green Chem.* **2014**, *16*, 1351−1357.
(112) Ethiraj, J.; Bonino, F.; Lamberti, C.; Bordiga, S. H_2S interaction with HKUST-1 and ZIF-8 MOFs: A multitechnique study. *Microporous Mesoporous Mater.* **2015**, *207*, 90−94.
(113) Bonino, F.; Lamberti, C.; Bordiga, S. IR and Raman Spectroscopies Probing MOFs Structure, Defectivity, and Reactivity. In *The Chemistry of Metal−Organic Frameworks*; Kaskel, S., Ed.; Wiley-VCH: Weinheim, Germany, 2016; pp 657−690.
(114) Srivastava, A.; Singh, V. B. Theoretical and experimental studies of vibrational spectra of naphthalene and its cation. *Indian J. Pure Appl. Phys.* **2007**, *45*, 714−720.
(115) Rekha, T. N.; Umadevi, M.; Rajkumar, B. J. M. Structural and spectroscopic study of adsorption of naphthalene on silver. *J. Mol. Struct.* **2015**, *1079*, 155−162.
(116) Horcajada, P.; Gref, R.; Baati, T.; Allan, P. K.; Maurin, G.; Couvreur, P.; Ferey, G.; Morris, R. E.; Serre, C. Metal-Organic Frameworks in Biomedicine. *Chem. Rev.* **2012**, *112*, 1232−1268.
(117) Choi, S.; Drese, J. H.; Jones, C. W. Adsorbent Materials for Carbon Dioxide Capture from Large Anthropogenic Point Sources. *ChemSusChem* **2009**, *2*, 796−854.
(118) D'Alessandro, D. M.; Smit, B.; Long, J. R. Carbon Dioxide Capture: Prospects for New Materials. *Angew. Chem., Int. Ed.* **2010**, *49*, 6058−6082.
(119) Alvarez, A.; Bansode, A.; Urakawa, A.; Bavykina, A. V.; Wezendonk, T. A.; Makkee, M.; Gascon, J.; Kapteijn, F. Challenges in the Greener Production of Formates/Formic Acid, Methanol, and DME by Heterogeneously Catalyzed CO_2 Hydrogenation Processes. *Chem. Rev.* **2017**, *117*, 9804−9838.
(120) Vitillo, J. G.; Smit, B.; Gagliardi, L. Introduction: Carbon Capture and Separation. *Chem. Rev.* **2017**, *117*, 9521−9523.
(121) Couck, S.; Denayer, J. F. M.; Baron, G. V.; Remy, T.; Gascon, J.; Kapteijn, F. An Amine-Functionalized MIL-53 Metal-Organic Framework with Large Separation Power for CO_2 and CH_4. *J. Am. Chem. Soc.* **2009**, *131*, 6326−6327.
(122) Furukawa, H.; Yaghi, O. M. Storage of Hydrogen, Methane, and Carbon Dioxide in Highly Porous Covalent Organic Frameworks for Clean Energy Applications. *J. Am. Chem. Soc.* **2009**, *131*, 8875−8883.
(123) Phan, A.; Doonan, C. J.; Uribe-Romo, F. J.; Knobler, C. B.; O'Keeffe, M.; Yaghi, O. M. Synthesis, Structure, and Carbon Dioxide Capture Properties of Zeolitic Imidazolate Frameworks. *Acc. Chem. Res.* **2010**, *43*, 58−67.
(124) Li, J. R.; Ma, Y. G.; McCarthy, M. C.; Sculley, J.; Yu, J. M.; Jeong, H. K.; Balbuena, P. B.; Zhou, H. C. Carbon dioxide capture-related gas adsorption and separation in metal-organic frameworks. *Coord. Chem. Rev.* **2011**, *255*, 1791−1823.
(125) Sumida, K.; Rogow, D. L.; Mason, J. A.; McDonald, T. M.; Bloch, E. D.; Herm, Z. R.; Bae, T. H.; Long, J. R. Carbon Dioxide Capture in Metal-Organic Frameworks. *Chem. Rev.* **2012**, *112*, 724−781.
(126) Wade, C. R.; Dinca, M. Investigation of the synthesis, activation, and isosteric heats of CO_2 adsorption of the isostructural series of metal-organic frameworks $M_3(BTC)_2$ (M = Cr, Fe, Ni, Cu, Mo, Ru). *Dalton Trans.* **2012**, *41*, 7931−7938.
(127) Ethiraj, J.; Albanese, E.; Civalleri, B.; Vitillo, J. G.; Bonino, F.; Chavan, S.; Shearer, G. C.; Lillerud, K. P.; Bordiga, S. Carbon Dioxide Adsorption in Amine-Functionalized Mixed-Ligand Metal-Organic Frameworks of UiO-66 Topology. *ChemSusChem* **2014**, *7*, 3382−3388.
(128) Seoane, B.; Coronas, J.; Gascon, I.; Benavides, M. E.; Karvan, O.; Caro, J.; Kapteijn, F.; Gascon, J. Metal-organic framework based mixed matrix membranes: a solution for highly efficient CO2 capture? *Chem. Soc. Rev.* **2015**, *44*, 2421−2454.
(129) Rodenas, T.; Luz, I.; Prieto, G.; Seoane, B.; Miro, H.; Corma, A.; Kapteijn, F.; Llabrés i Xamena, F. X.; Gascon, J. Metal-organic framework nanosheets in polymer composite materials for gas separation. *Nat. Mater.* **2015**, *14*, 48−55.
(130) Benzaqui, M.; Pillai, R. S.; Sabetghadam, A.; Benoit, V.; Normand, P.; Marrot, J.; Menguy, N.; Montero, D.; Shepard, W.; Tissot, A.; Martineau-Corcos, C.; Sicard, C.; Mihaylov, M.; Carn, F.; Beurroies, I.; Llewellyn, P. L.; De Weireld, G.; Hadjiivanov, K.; Gascon, J.; Kapteijn, F.; Maurin, G.; Steunou, N.; Serre, C. Revisiting the Aluminum Trimesate-Based MOF (MIL-96): From Structure Determination to the Processing of Mixed Matrix Membranes for CO_2 Capture. *Chem. Mater.* **2017**, *29*, 10326−10338.
(131) Masala, A.; Vitillo, J. G.; Mondino, G.; Grande, C. A.; Blom, R.; Manzoli, M.; Marshall, M.; Bordiga, S. CO_2 Capture in Dry and Wet Conditions in UTSA-16 Metal-Organic Framework. *ACS Appl. Mater. Interfaces* **2017**, *9*, 455−463.

DOI: 10.1021/acs.inorgchem.8b03087
Inorg. Chem. 2019, 58, 1607−1620

(132) Sabetghadam, A.; Liu, X. L.; Benzaqui, M.; Gkaniatsou, E.; Orsi, A.; Lozinska, M. M.; Sicard, C.; Johnson, T.; Steunou, N.; Wright, P. A.; Serre, C.; Gascon, J.; Kapteijn, F. Influence of Filler Pore Structure and Polymer on the Performance of MOF-Based Mixed-Matrix Membranes for CO_2 Capture. *Chem. - Eur. J.* **2018**, *24*, 7949−7956.
(133) Sabetghadam, A.; Liu, X. L.; Orsi, A. F.; Lozinska, M. M.; Johnson, T.; Jansen, K. M. B.; Wright, P. A.; Carta, M.; McKeown, N. B.; Kapteijn, F.; Gascon, J. Towards High Performance Metal-Organic Framework-Microporous Polymer Mixed Matrix Membranes: Addressing Compatibility and Limiting Aging by Polymer Doping. *Chem. - Eur. J.* **2018**, *24*, 12796−12800.
(134) Herzberg, G. *Molecular Spectra and Molecular Structure*; van Nostrand Reinhold: New York, 1950.
(135) Shearer, G. C.; Forselv, S.; Chavan, S.; Bordiga, S.; Mathisen, K.; Bjorgen, M.; Svelle, S.; Lillerud, K. P. In Situ Infrared Spectroscopic and Gravimetric Characterisation of the Solvent Removal and Dehydroxylation of the Metal Organic Frameworks UiO-66 and UiO-67. *Top. Catal.* **2013**, *56*, 770−782.
(136) Bonelli, B.; Civalleri, B.; Fubini, B.; Ugliengo, P.; Arean, C. O.; Garrone, E. Experimental and quantum chemical studies on the adsorption of carbon dioxide on alkali-metal-exchanged ZSM-5 zeolites. *J. Phys. Chem. B* **2000**, *104*, 10978−10988.
(137) Garrone, E.; Bonelli, B.; Lamberti, C.; Civalleri, B.; Rocchia, M.; Roy, P.; Otero Areán, C. Coupling of framework modes and adsorbate vibrations for CO_2 molecularly adsorbed on alkali ZSM-5 zeolites: Mid- and far-infrared spectroscopy and ab initio modeling. *J. Chem. Phys.* **2002**, *117*, 10274−10282.
(138) Kim, D.; Park, J.; Kim, Y. S.; Lah, M. S. Temperature dependent CO_2 behavior in microporous 1-D channels of a metal-organic framework with multiple interaction sites. *Sci. Rep.* **2017**, *7*, 41447.
(139) Pazé, C.; Bordiga, S.; Lamberti, C.; Salvalaggio, M.; Zecchina, A.; Bellussi, G. Acidic properties of H-beta zeolite as probed by bases with proton affinity in the 118−204 kcal mol^{-1} range: A FTIR investigation. *J. Phys. Chem. B* **1997**, *101*, 4740−4751.
(140) Bordiga, S.; Lamberti, C.; Bonino, F.; Travert, A.; Thibault-Starzyk, F. Probing zeolites by vibrational spectroscopies. *Chem. Soc. Rev.* **2015**, *44*, 7262−7341.

DOI: 10.1021/acs.inorgchem.8b03087
Inorg. Chem. 2019, 58, 1607−1620